The Gemini-North Multiobject Spectrograph Optical Performance

Richard Murowinski[a], J.R. Allington-Smith[b], D. Crampton[a], R. Davies[b], M. Fletcher[a], D. Henry[c], I.M. Hook[d], I. Jørgensen[e], S. Juneau[a], C. Morbey[a], J. Stilburn[a], K. Szeto[a].

[a]National Research Council of Canada, Herzberg Institute of Astrophysics, 5071 West Saanich Road, Victoria, BC, V9E 2E7, Canada
[b]Department of Physics, Science Laboratories, University of Durham, South Road, Durham, DH1 3LE, U.K.
[c]UK Astronomy Technology Centre, Royal Observatory, Edinburgh, Blackford Hill, Edinburgh, EH9 3HJ, U.K.
[d] Department of Physics, University of Oxford, Nuclear & Astrophysics Laboratory, Keble Road, Oxford OX1 3RH, U.K.
[e]Gemini Observatory, 670 N. A'ohoku Place, Hilo, Hawaii, 96720, USA

ABSTRACT

The Gemini Multiobject Spectrographs (GMOS) were designed to take advantage of the exquisite image quality expected of the Gemini telescopes. To achieve this, two of the many requirements placed on the optical system was that it not degrade the best image quality expected of the telescope by more than 10% while delivering a throughput of about 80% over the entire 0.4-1 μm waveband. In this paper, key components of the design and execution of this optical system are discussed and test results are presented demonstrating that it meets these requirements on Gemini today. Among other characteristics, we look at the image quality performance as a function of colour and field angle, the measured throughput, and the focalplane flatness on the detectors.

Keywords: spectrograph, optical instrumentation

1. INTRODUCTION

The Gemini Observatories project came into being more than a decade ago with the objective of providing 8 metre class telescope facilities to the partner countries. A niche upon which Gemini focussed its attention was to deliver unprecedented image quality with its large aperture. From the start, Gemini designers realized that this objective would only be achieved within the modest budget available through setting uniform and balanced performance requirements for all aspects of the observatory, including the telescope, enclosure and instrumentation.

Among the first suite of instruments commissioned for Gemini were the two GMOSs: workhorse optical spectrographs meant to satisfy the needs of a wide range of observational studies,[1] including optical imaging, long slit spectroscopy, multislit spectroscopy and integral field spectroscopy. The bulk of the work of developing the GMOSs was assigned[2] to a collaboration of the Particle Physics and Astronomy Research Council of the UK, and the National Research Council of Canada. It is the development and performance of the first GMOS optical system, and how it plays its part in establishing Gemini into that niche by providing exquisite image quality and high throughput, which we will take a brief look at in this small screed.

Further author information: (Send correspondence to R.G.M.)
R.G.M.: E-mail: Richard.Murowinski@nrc.ca, Telephone: 250 363 0057

2. REQUIREMENTS AND DEVELOPMENT PLAN

GMOS was designed and built concurrent with the design and fabrication of the Gemini telescopes. Indeed, one of the requirements placed on the telescope was to not degrade the 10th percentile best seeing by more than 15%, and one of those on GMOS was to not degrade the telescope delivered image quality (IQ) by more than 10%.[3] That basic statement, together with requirements for slit throughput and for imaging the slits sufficiently well, were extended into an expression of the required final 50% and 85% Encircled Energy Diameter (EED), on axis and at the edge of the field, at three representative wavelengths: 370, 550 and 1000nm. Taken together, the main requirements which guided the design and testing of the GMOS optics are summarized in Table 1.

Table 1: The requirements placed on the Northern GMOS optics

50% EED on-axis	0.103, 0.092 and 0.079 arcseconds at 370, 550 and 1000nm respectively
85% EED on-axis	0.180, 0.180 and 0.176 arcseconds at 360, 550 and 1000nm repsectively
Field	5.5x5.5 arcminute, limited to 7 arcminute diameter
Wavelength Range	0.4 - 1.1 μm, with goal of extending to 0.36 and 1.8 μm
Optical Throughput	80% (not including grating, filter or detector)
Minimum slit width	as small as 0.20 arcseconds
Spectral Resolution	R=5000 to R=500 with 0.5 arcsecond slits
Image Scale	0.072 arcsecond per 13.5 μm pixel
Optical distortion	$<$ 0.1% at edge of field
Ghosting	minimize parasitic light
Operating temperature	-5C to +5C

Once an optical design comfortably met the above requirements on paper (see below), the room available between the spec and the modelled optical performance was further partitioned to allow 10% for tolerancing and 0.034 arcseconds each for $\lambda/8$ grating flatness and $\lambda/4$ filter transmitted wavefront error. The remaining budget was allocated to dynamic effects when mounted on the telescope such as image movement due to gravity.

In the GMOS collaboration, the Herzberg Institute of Astrophysics (HIA) was assigned the responsibility for delivering optical barrels to the integration and test facility at UK Astronomy Technology Centre (UKATC).[4] Optical blanks were purchased from a number of sources and sent to an optical fabrication company for processing into lenses. The remaining work on the optical barrels was done at HIA: fabricating cells and mounting components, installing and aligning the lenses into barrels, and testing the barrels. After individual performance and environmental tests were successfully completed, the barrels were shipped to UKATC where they were integrated with the rest of the instrument, including grating and filters, and where the optical system underwent performance tests as part of the whole instrument.

2.1. Overall Optical Design

A refracting type spectrograph such as GMOS[1] comprises three main components that work closely together. First of all it is necessary to collimate the light from the telescope focal surface (where the slit mask is located) so that an image of the telescope pupil is positioned where the second component, a grating, can diffract the desired wavelength bandpass most effectively. The third component, a camera, provides an image of the telescope focal surface with its slit-mask covering the field of view.

Due to the wide wavelength and throughput goals, and since GMOS is restricted in overall length according to the mechanical space allocation, a three-component collimator was chosen and special glasses needed to be selected. It soon became apparent that the glass manufacturers were undergoing a major reduction of glass types available from their earlier catalogues. Not only that, well-known glass types were replaced with environmentally friendly alternatives. During this time GMOS optics underwent a number of design revisions to accomodate these changes. Unfortunately, the final design required calcium fluoride elements at a diameter of 300 mm, whose delivery was problematic. Initially concerned about this, we were eventually assured that it could be achieved with the required homogeneity.

2.2. Collimator Design

The requirements for GMOS stated that the instrument should be driven by spectrographic rather than imaging performance and so the collimator was designed to image a flat slit plane rather than the curved focal surface of the telescope. A perfect f/16 beam with properly placed exit pupil position was used as optical input to the design. This approach does not allow for the introduction of telescope aberrations and so in the optimisation of the collimator no effort was made to balance out those aberrations. Hence the uniformity of image quality as a function of field angle is slightly degraded in imaging mode (discussed in more detail below). This slight limitation is corrected by the GMOS atmospheric dispersion corrector (ADC), which when commissioned will flatten the telescope-delivered field from a 1.91 to a 4.0 metre radius of curvature.

So, to begin with, the collimator design assumed the appropriate f/16 input beam, field of view, and colour bandpass range. Since the output of the collimator is effectively an image of the telescope pupil, optimisation can proceed by analyzing the field points produced by a paraxial lens set located appropriately in front of the pupil position. A compromise diameter of 98 mm was chosen for the pupil (grating); this size allowed for the use of standard grating sizes yet yields spectral resolutions adequate for most projects.

A diagram of the collimator is shown in Figure 1. There are 3 lens groups: first, a large triplet field lens, then a smaller triplet and finally a 4-element collimating combination. Such complexity is required to reach the requirements of field angle and initially specified colour correction. Because the instrument is primarily a spectrograph, all the light from each field point should overlap as closely as possible at the image of the pupil. The grating, then, will diffract light from any field point in exactly the same way since the same area of the grating is involved. Note that the 150mm diameter circular filters are located between the last lens group and the pupil position.

2.3. Camera Design

The function of the spectrograph camera is to receive the collimated light from the pupil and transform it into an image; the slit mask at the focal surface of the telescope is imaged at the camera focus. Every field point has associated with it, its own collimated beam. Input for the camera design made use of the output beams from the collimator with all collimator parameters remaining fixed. Because the beams diverge from the pupil position, the first camera lens must intercept them completely. When in spectrographic mode the beams can diverge at even greater angles than those from off-axis images because there are the added angles of diffraction. Each beam from each field angle at each colour needs to be focussed at the image plane at the proper distance from the axis according to the scale chosen. Figure 1 shows the configuration of the camera with its 2 quartets, triplet, and singlet field flattener. The latter forms the window of the detector cryostat. Because telecentricity was not as important a consideration as distortion and image flatness, the exit pupil was permitted to be as close as 363 mm from the focal plane inside the camera. This means that image positions in the focal plane shift position slightly when the images are out of focus.

2.4. Optical Design Summary

At a later stage of the development process the wavelength extension goals were dropped. However, since the glass for the optics was already purchased, optimisations after that time were better able to yield solutions within specifications, and at the same time to relax tolerances. It may be said that GMOS is over-designed for the exact final requirements. While this may be true, relaxed tolerances helped mitigate the risk of problems during instrument alignment, integration and test. In any case, it should be noted that GMOS optics can function from 350 to 1500nm if needed.

In summary, the collimator was designed first and then the output of the collimator was used as input for the design of the camera. This means that inherent aberrations remaining in the collimator after its design

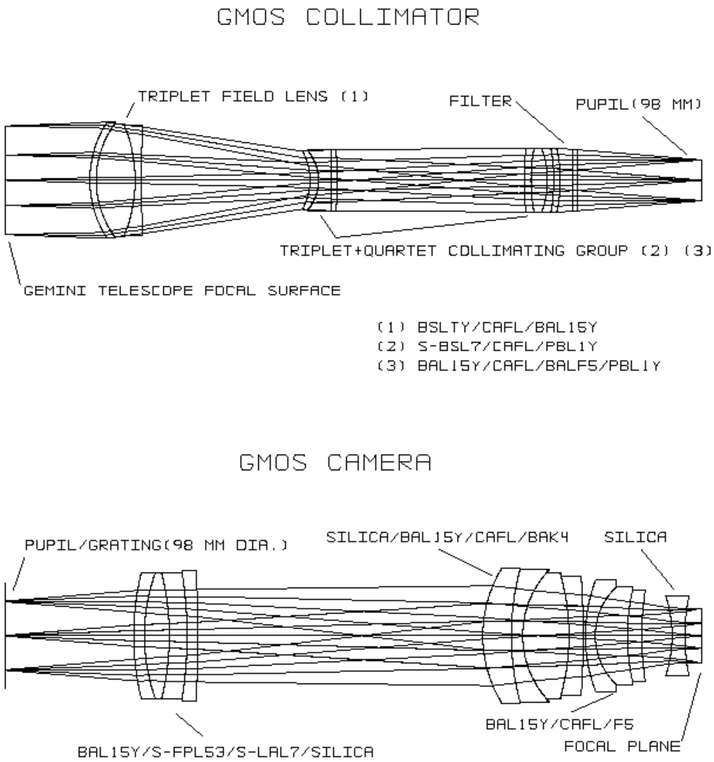

Figure 1. GMOS optical designs. The upper figure presents the collimator design, and the lower figure is that of the camera.

are compensated for, to some extent, in the camera. No residual aberrations from the telescope optics are compensated for in either the collimator or the camera.

It should also be noted that all collimator and camera optics were designed for the temperatures and pressures expected on Cerro Pachon and Mauna Kea. Refractive indices of the glasses are significantly different for these conditions so that changes needed to be made for testing purposes closer to sea level. Whereas nominal catalogue values of refractive indices were used in all the preliminary design work, the final design made use of particular refractive indices obtained from the manufacturer in their accompanying melt data.

2.5. Mechanical design

The main optical elements are divided into a total of six groups, three in the collimator barrel and three in the camera barrel. Each lens group is an assembly of three to four lenses and their lens cells, with each lens in a unique cell. Except for the calcium fluoride lens, each lens cell has an inner cell and an aluminium outer cell. The inner cell material is determined by matching the coefficient of thermal expansion (CTE) of the cell metal to the glass. For GMOS, the inner cell materials used are copper, Invar and titanium. All outer cells are made with aluminium. The calcium fluoride lenses have only a single aluminium cell which has similar coefficients of thermal expansion to that glass. The lenses are stacked and fastened together by their aluminium cells for each lens group. At room temperature, the gap between two lenses within a group is 50 μm, nominally. For each lens group, the cells are designed to have cross-sectional geometry that axially athermalized the lens separations. The inner and outer cells are bonded together with Summers Optical Milbond adhesive. The gap between the inner and outer cells is calculated such that the sectional area of the adhesive is maintained throughout the design temperature range, therefore the inner cell experiences minimal thermal strain. The design approach has been described earlier.[5]

The radial athermalization and support between the lens and its cell is achieved by using flexures. The flexures are bonded tangentially between the inner diameter of the inner cell and the outer diameter of the lens with the same Milbond adhesive. The number of flexures for each lens is determined to ensure sufficient the radial and axial stiffness, and some of the heavier lenses require two rows of flexures for support. The flexure materials are also chosen according to the CTE of the glasses; they include stainless steel, aluminium and brass. Additional FEA analysis was performed to verify that the finger flexure design has no localized effects on the stress level and figuring of the lens. Moreover, this mounting technique allows precise alignment between the optical axis of the lens and the mechanical axis of its cell, independent of the mechanical axis of the lens. The gap between the lens and its cell is 2 mm nominally but may vary slightly according to the alignment tolerance between the optical and mechanical axes of each lens. After all the lenses of a group are mounted, they are then stacked and aligned with respect to the mechanical axes of their cells. The group is then pinned for positional repeatability at reassembly.

Each of the 2 mm gaps between the lens and its cell is filled with RTV rubber. The RTV rubber and an O-ring placed between two lens cells seal the volume, as defined by the $50\mu m$ gap. The gap is filled with Cargille 3421 laser liquid, an optical couplant with the suitable refractive index and transmission over the operational wavelength range. After filling, each lens group is treated inside a vacuum chamber to eliminate any trapped air. The volumetric change due to temperature is accommodated by a bladder system, one for each lens pair interface. The hydrostatic pressure of the couplant on the lens is also checked against the stress level, figuring and overall displacement for each lens group. The bladder is a thin vinyl rubber reservoir, one side of which is exposed to atmospheric pressure; thus altitude change has no effect on the differential pressure between atmosphere and the lens group.

A two-layer of sol-gel over magnesium fluoride antireflection (AR) coating[6] is applied to the two exterior surfaces of each group. The lenses are delivered from the manufacturer with group external surfaces coated with magnesium fluoride. The sol-gel overcoat is applied at HIA. Chemical compatibilities among the coating, optical couplant, RTV rubber, O-ring material, Milbond adhesive and the vinyl bladder have been checked and verified experimentally.

Each group is attached to the barrel via three shim-pucks which allow its orientation, such as tip/tilt and focus, to be adjusted during the optical alignment process. The overall optical axis is defined by the mechanical axis of the barrels, to which the mechanical axes of the lens groups are aligned. Once the optics are aligned, the lens groups are pinned to the barrel for positional repeatability at reassembly. The bladder system including its plumbing, vinyl rubber reservoirs and their protective metal casings are attached to the aluminium barrel.

3. LAB TEST RESULTS

3.1. IQ in the lab

Image quality was measured on the assembled and aligned optical barrels as part of their tests before shipping to the GMOS integration center. The measurement was made by illuminating the optics, aligned on optical benches and at standard pressure and temperature, through a $10\mu m$ pinhole located at the collimator input focus. The output image was sampled with an SBIG lab camera which has $9\mu m$ pixels (0.048 arcsecond/pixel at the camera focus) and wavelength was varied by changing the 10nm bandpass source colour filter. The system was refocused at each wavelength.

The resultant images were processed with IRAF function *psfmeasure* to get the 0.5 and 0.85 EED. They were not corrected for the very slight overestimate of PSF due to the pinhole diameter, nor that due to the spatial undersampling of the images. Results, seen in Figure 2, comfortably meet the spec given in Table 1 over most of the passband, with performance degrading to about spec level at the 1000nm limit.

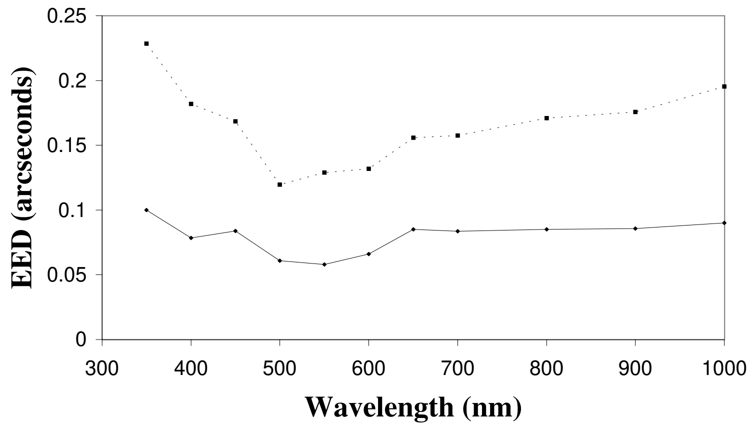

Figure 2: GMOS image quality measured in the lab. The solid line is 50% EED, and the dotted line is 85% EED.

3.2. Focus as a function of wavelength, filter and temperature

Focus change as a function of temperature and wavelength was measured at HIA. A series of filters were used to control the colour of light illuminating the source pinhole, as in the setup described above. The on-axis focal position as a function of wavelength, seen in Figure 3, agrees nicely with the Zemax model. Focus change with temperature was measured during the optical barrel cold tests and found to be about 120 μm over the operational range of -5C to +5C.

Instrument focus with changes of wavelength and temperature were remeasured after the optics were integrated into the instrument at UKATC. This was also done using the GMOS science filters and grating to characterize fixed focus offsets in each element as a result of introduced transmitted wavefront error (TWE), which might contribute some small amount of unwanted optical power. The first set of filters we received from Barr Associates proved to be out of spec in TWE, and resulted in significant defocus. Barr undertook to remake the filters, and produced a set which were much better, conforming nicely to the measured curve (the open circles in Figure 3) in all except the g band.

With the instrument fully assembled, we found there was no consistently measurable change of focus with temperature over the operational range. That this is different from the earlier measurement on the bare optical barrels can be explained by the different materials that were used in the structure between the collimator and the mask, and between the camera barrel and the cyrostat window. The instrument control software automatically adjusts camera focus to keep the spectrograph in focus based on the chosen central wavelength, filter and grating, but does not attempt to adjust focus for changes in ambient temperature.

3.3. Focal flatness

The flatness of the focal surface at the detector is a critical parameter. Simulations with Zemax predicted that the surface of best focus would be dish-shaped, concave to the sky direction, with a difference between the center and edge of the imaging field (i.e. sagittal depth, or sag) of 70μm, depending on the exact criterion used to define the best focus. The shape, but not the absolute best focus value, was predicted to be invariant with wavelength. In the camera beam of f/4.8 this amounts to a maximum geometric blur of 7 μm, roughly equivalent to a two-dimensional gaussian function with 5 μm 0.5EED. This projects to 27 milliarcseconds on

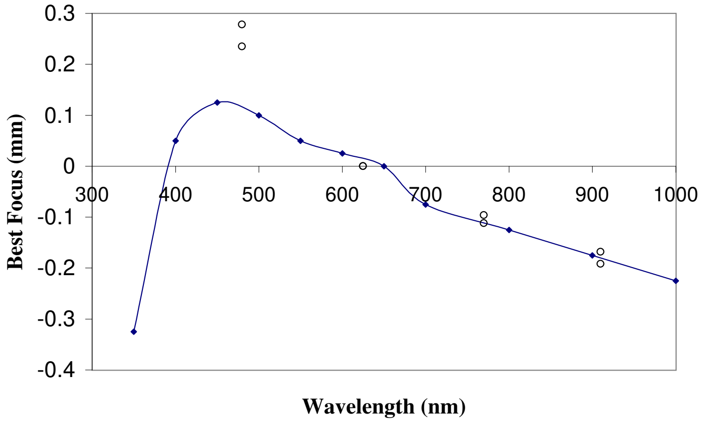

Figure 3. GMOS focus, measured in the lab. The solid line is the measurement of focus change with wavelength during barrel subassembly tests. The open circles indicate the best imaging focus value after instrument assembly, in each of the science filters : two each of g,r,i and z. The deviation of the g filters is probably a result of its larger transmitted wavefront error.

the sky and represents a broadening of the PSF describing the image quality assigned in the error budget to the post-slit optics, of between 3.4 and 5.7% depending on wavelength. It was therefore predicted to be a negligible contribution to the PSF.

The shape of the focal surface was measured by imaging a mask containing a 21 by 21 matrix of small pinholes covering the full mask field, using filtered light to eliminate the effect of the variation of focus with wavelength. The detector translation stage was stepped along the optical axis through the previously determined on-axis focus setting in small increments. A script which called the IRAF *imexamine* task was used to measure the FWHM of each spot over the full field. From the FWHM measured for each spot at different translations along the optical axis, the best focus was determined by fitting a parabola to the data using a specially-written IDL program. The results were then examined to reveal the overall tilt of the focal surface and its center-edge sag.

The center-edge sag was found to be about $70\mu m$ as predicted, but initially the tilt exceeded the tolerance, adopting $\pm 50\mu m$ as the maximum allowable variation in focus from one edge to the other. Although this could have been caused by an error in the angular alignment of the CCD mosaic during installation in the cryostat, it could also have been due to a translation of the cryostat window orthogonal to the optical axis since it has optical power. The latter option was thought to be more likely since no particular attempt had been made to center the window accurately to the optical axis during installation. Even if it was the detector installation which was at fault, moving the cryostat window is an acceptable method of correcting it since Zemax simulations show that such a translation could correct the tilt of the focal surface without significantly degrading the PSF. From the Zemax model, an approximately linear relationship between tilt and window shift was derived and used to predict the required window translation. When this was performed the focal surface tilt was found to be acceptable. Measurement of the initial tilt and the value after correcting the position (Oct 2000) of the window are shown in Table 2. The other dates refer to episodes of major instrument disassembly and reassembly - for example, the 27 June 2001 measurement was made after the instrument was reassembled after shipment to the observatory summit. It can be seen that the tilt of the focal surface is repeatable under these operations. The shape of the focal surface is shown in Figure 4.

Table 2: Maximum deviations in focus due to the tilt of the focal surface with respect to the detector.

Date	Max focus shift at X edge (μm)	Max focus shift at Y edge (μm)
Original	146	72
After Correction	23	21
27 Jun 2001	18	23
13 Oct 2001	18	18
29 Mar 2002	6	18

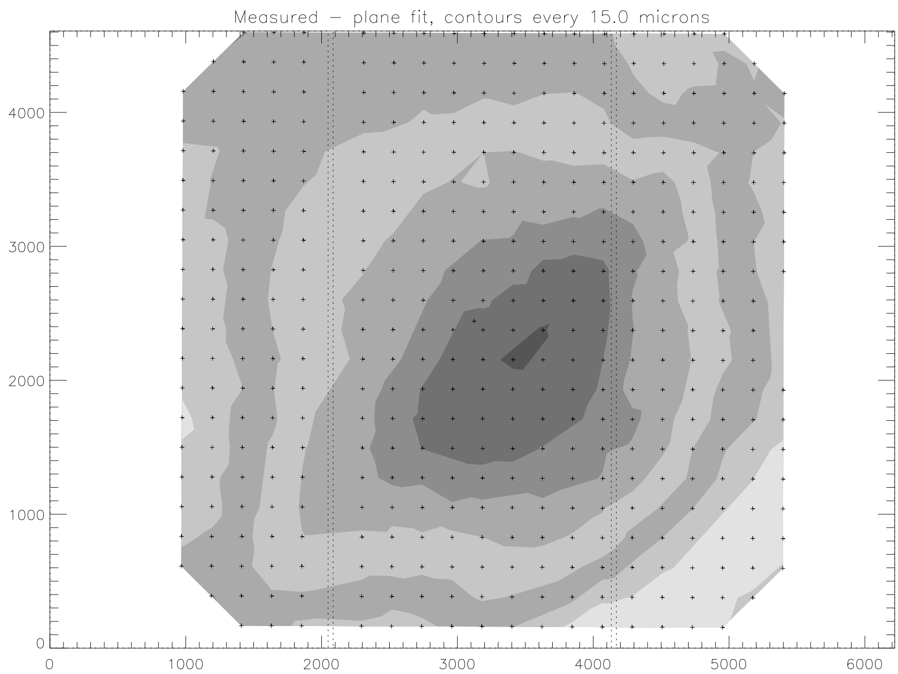

Figure 4. A contour map of the 5.5 by 5.5 arcminute focal surface after adjustment of the window position and with the residual tilt subtracted off. The axes are in pixel units with dispersion aligned with the horizontal (x) axis. The gaps between the CCD chips are indicated. The small crosses mark the locations of images of the pinholes. The shaded contours have an interval of $15\mu m$.

3.4. Instrumental IQ over the field

The instrumental IQ over the field was measured by imaging the same pinhole mask described above. The data in Figure 5 were taken through the GMOS i filter, with GMOS mounted on the telescope (i.e. the temperature and atmospheric pressure were at design values) and using the facility calibration unit as the illumination source. The GMOS focus was set to a the value that gives the best average focus over the field. The IQ values plotted are 50% (solid symbols) and 85% (open symbols) EED, corrected for the pinhole size. All measurements demonstrate performance within specification.

3.5. Throughput

Optical throughput was measured in quite a straightforward way. The optics were illuminated with a stable pinhole source, and a calibrated silicon photodiode was used to measure the flux entering and then exiting the

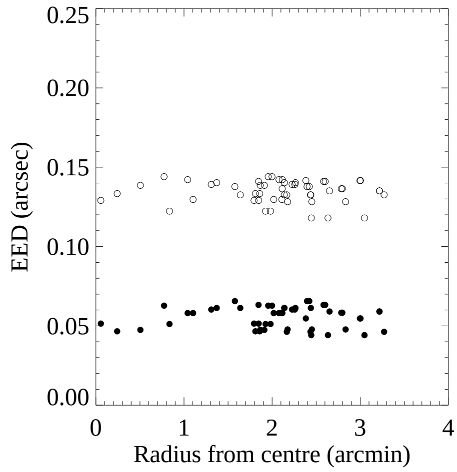

Figure 5. GMOS intrinsic image quality as a function of radial distance, measured on the telescope by illuminating a pinhole mask from the Gemini calibration source. Closed circles are 0.5EED, open circles 0.85EED. These numbers represent the final delivered instrument performance, taken at the design temperature and pressure, and corrected for input PSF.

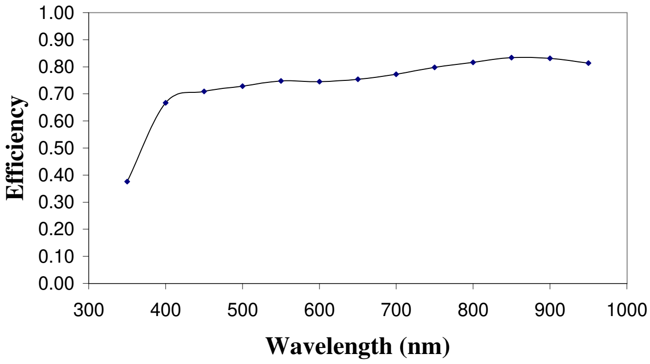

Figure 6: GMOS optical efficiency, as measured in the lab, excluding filters, grating or detector efficiency.

optics at the camera focus, the values of which were then ratioed. The beam leaving the source pinhole was stopped down to something slower than the f/16 collimator input, and the source photodiode was situated so that it completely intercepted the source flux over its 1 cm^2 active surface. The values shown in Figure 6, then, do not include the GMOS filters, grating (or mirror), ADC nor the CCD efficiency. They do include the cryostat window. On-sky measurement of instrument throughput taken during commissioning can be found elsewhere in these proceedings,[4] and are reasonably consistent with these numbers.

3.6. Hartmann focus

Focusing of GMOS was done using focus runs (minimizing image size as a function of instrument focus) and also using a pair of Hartmann masks in the forward filter wheel, which is in the collimated beam. The Hartmann focus procedure involves measuring spot positions with each of the two Hartmann masks in the beam in turn - the separation being approximately proportional to the amount of defocus. The constant of proportionality was found to be 136.6 μm of focus per pixel of image separation. Typically a second iteration was carried out to confirm that the spot separation was negligible with respect to the measurement uncertainty (about 0.04 pixels, corresponding to 5 μm). In general, the left-right pair of Hartmann masks are used to focus the instrument, although one could also use an up-down pair of masks, also found in the forward filter wheel.

3.7. Grating resolution

The resolving power obtained with our 600/mm grating was checked in the instrument using a mask containing a long slit (nominal width 0.5 arcseconds) illuminated by a mercury discharge lamp and diffuser. A direct image of the slit was 7.35 pixels wide at FWHM, equivalent to 0.53 arcseconds projected on the sky.

The dispersed image was examined using the IRAF *imexamine* task to yield line positions and widths. A good linear fit between the measured emission line positions and wavelength was obtained with dispersion 0.04528 nm/pixel with an uncertainty of 0.1nm RMS. This is within 1% of the predicted value. The central wavelength was 414nm. Each line was found to have a FWHM of 6.0 ± 0.2 pixels, different from that in the direct image due to the anamorphic effects of the non-Littrow mounting of the grating, as expected. This gives a wavelength resolution $\delta\lambda = 0.2717$ (± 0.009) nm, compared with the prediction of 0.2789nm for a slit width of 0.53 arcseconds, slightly better than expected.

However, the wavelength resolution appears to be less than this (i.e. the resolving power, $R = \frac{\lambda}{\delta\lambda}$ is greater) if one uses a FWHM obtained from a gaussian fit (as given by *imexamine*). In this case the measured resolution is 0.2567nm. This difference is due to the fact that the slit image resembles a top-hat more closely than a gaussian function, and the gaussian fit underestimates the FWHM of the actual slit profile. Overall, it is clear that the spectral resolution is very close to expectation, with its precise value depending on the criterion used to define the resolution and the details of how it is measured. Measurements of this and other gratings are summarised in Table 3. The uncertainty in the resolving power ratio arises from errors in measuring the line width and amount to ±3%. The results confirm the conclusion reached above.

Table 3. A comparison of predicted and measured dispersion and resolving power for a number of GMOS diffraction gratings.

Grating	Dispersion (nm/pix)		R(actual/predicted)	
	predicted	measured	gaussian fit	top-hat fit
R150	0.174	0.1776	1.06	0.93
R400	0.068	0.0668	1.15	1.00
B600	0.047	0.0453	1.09	1.03
R831	0.034	0.0337	1.12	0.94

4. TELESCOPE RESULTS

4.1. IQ over the field

As described earlier, the telescope delivers a focal surface with a 1.91 metre radius of curvature, while the input field to GMOS is flat in order to best image the flat slitmasks. Further, when the ADC is mounted in front of the input field, it would deliver a 4 metre radius of curvature. Hence a compromise needs to be found in focussing the telescope to GMOS which best meets these conditions. The design compromise chosen was to build the

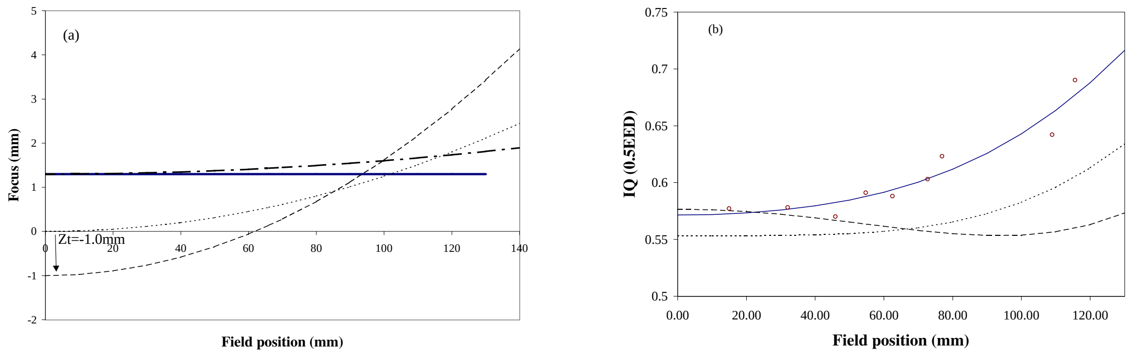

Figure 7. (a) represents the focal surfaces of the telescope over the 3.5 arcminute radius. The GMOS mask plane is shown as a solid line, the OIWFS focal surface as a dash-dot and the ADC focal surface at nominal telescope focus as a dotted line. The dashed line depicts the non-ADC focal surface with telescope focus offset to $Z_T = -1$mm. In (b) we see image quality over the (non-ADC) field, as measured on the sky at the GMOS detector focus. The data points are measured PSF. The solid line represents a best fit of the model to the data: the PSF variation for an absolute focus $Z_T = +3.33$mm and 0.5EED intrinsic IQ = 0.55 arcseconds (0.5EED). The dotted and dashed lines show the modelled PSF variation for an on-axis focus ($Z_T = +1.27$mm) and best non-ADC compromise focus ($Z_T = -1.00$mm) using the same intrinsic PSF of 0.55 arcseconds.

maskplane 1.27mm closer to the telescope than the on-axis focus, placing it at the best average focus with the ADC in place and with the telescope at nominal focus: on-axis focal surface 300.0 mm from the instrument mounting surface (which we define as telescope focus $Z_T = 0$mm). When the ADC is not mounted, the best average focus is achieved by offsetting the telescope focus 1mm into the instrument to $Z_T = -1$mm. The mask plane, properly focussed ADC focal surface and offset non-ADC surface are depicted in the left pane of Figure 7. The primary focus reference is the on-instrument wavefront sensor (OIWFS), which itself travels on a spherical surface with a 16.5 metre radius of curvature due to the need to point to the center of the telescope secondary mirror. The OIWFS probe control software reports the focus offset between the sensor focal position and the telescope focal surface at $Z_T = 0$, evaluated at the field angle of the guide star. This value is then subtracted from the focus errors measured by the OIWFS's Shack-Hartmann sensor to arrive at true telescope focus error.

The image quality degradation resulting from defocus in this f/16 system can be estimated in a simple manner from the focus offset. Since the defocus contribution to the 0.5EED PSF can be estimated as 0.7 times the geometric blur diameter, the 0.5EED size of the defocus blur is approximately $0.7 \times defocus \times platescale/16$. This value is then summed in quadrature with the best focussed 0.5EED image quality to get an estimate of the expected 0.5EED size with defocus. In the right pane of Figure 7, the dashed line indicates the expected PSF change over the field without an ADC in place and telescope at best compromise focus: $Z_T = -1$mm. The dotted line represents PSF if the telescope were focussed onto the mask plane on-axis, i.e. with $Z_T = +1.27$mm.

Fields suitable for image quality analysis were imaged during the commissioning period, without the ADC in place. Those data represented among the best image quality achieved to date with GMOS on Gemini, and were used to study how well the telescope was focussed to GMOS by examining how the data fit the above relationships. Note that numbers used here are the measured 0.5EED; the measured FWHM in the same i-band data are about 0.45 arcseconds, the difference being the result of a slightly non-gaussian image profile.

Figure 7 shows in the right pane the measured image quality in data taken in i-band, plotted as a function of distance from the field center. During this observation, the OIWFS was guiding on a star at about 66mm of field angle and near the annulus where OIWFS focus correction is null, hence any uncertainty in OIWFS focus tracking, which indeed had not yet been characterized when these data were taken, is not a significant contribution to this analysis. The solid line shows a fit to the observed data, which corresponds to a focus of

$Z_T = +3.33$mm and intrinsic telescope IQ of 0.55 arcseconds. We can see from this analysis that these images were taken with the telescope focussed about 4.33mm short of the best average focus and 2.06mm short of the on-axis focus.

Over this same range of Z_T, the modelled on-axis IQ varies only a small amount: 0.577 arcseconds for the best compromise focus, 0.553 arcseconds for the on-axis focus and 0.571 for the fit to the measured data. Under the changing atmospheric conditions of real telescope operations, it would be extremely difficult using an on-axis focus run to correctly focus the telescope to the point which gives best average IQ over the field. Fitting the image quality function over the field gives much more robust results, and is obviously a preferred method of determining the telescope focus offset for GMOS.

4.2. Ghost and Scattered Light

Considerable attention was paid in the optical design to ensure that parasitic and scattered light was kept to a minimum. The CCD detector surface is relatively reflective (at some wavelengths more than others) and light returning from the detector can be scattered back again from one or more of the lenses. Careful optical design, baffles and very efficient AR coatings on the GMOS optics help reduce such effects. No ghosts arising from reflections of bright stars from other lens surfaces have been observed, although ghosts from the filters are apparent in part of the field at a level of about 0.1% of the parent object. The filters were originally tilted by 3 degrees in an attempt to avoid this problem, but subsequent ray tracing shows that a tilt of almost 6 degrees is necessary to completely eliminate them from the entire field. New holders that will increase the tilt of the filters are being manufactured.

REFERENCES

1. R.L. Davies, *et. al.* " GMOS: The GEMINI Multiple Object Spectrographs" in *Optical Telescopes of Today and Tomorrow: Following in the Direction of Tycho Brahe*, Arne Ardeberg, ed., *Proc. SPIE* **2871**, pp. 1099–1106, 1996.
2. D. Crampton, *et. al.* "Gemini multi-object spectrograph GMOS: integration and tests" in *SPIE Conference on Optical and IR Telescope Instrumentation and Detectors*, Masanori Iye and Alan F. Moorwood, eds., *Proc. SPIE* **4008** pp. 114–122, 2000.
3. R. Murowinski, *et. al.* "The GEMINI Multiobject Spectrographs" in *SPIE Conference on Optical Astronomical Instrumentation*, Sandro D'Odorico, ed., *Proc. SPIE* **3355**, pp. 188–195, 1998
4. I. Hook, *et. al.* "The Gemini-North Multiobject Spectrograph Integration, Test and Commissioning", this conference, *Proc. SPIE* **4841**-185, 2002.
5. T. Bond, M. Fletcher and K. Szeto, "Gemini Multi Object Spectrograph Optomechanical Design" in *Optomechanical Design and Precision Instruments*, Alson E. Hatheway, ed., *Proc SPIE* **3132**, pp. 32–40, 1997
6. J.R. Stilburn, "High-efficiency sol-gel antireflection coatings for refractive optics" in *Optical and IR Telescope Instrumentation and Detectors*, *Proc SPIE* **4008**-150, 2000.